HIGH RESOLUTION IMAGING

Development of ultrasound bioprobe for biological imaging

Gajendra S. Shekhawat,[1]* Steven M. Dudek,[2] Vinayak P. Dravid[1]

We report the development of an ultrasound bioprobe for in vitro molecular imaging. In this method, the phase of the scattered ultrasound wave is mapped to provide in vitro and intracellular imaging with nanometer-scale resolution under physiological conditions. We demonstrated the technique by successfully imaging a magnetic core in silica core shells and the stiffness image of intracellular fibers in endothelial cells that were stimulated with thrombin. The findings demonstrate a significant advancement in high-resolution ultrasound imaging of biological systems with acoustics under physiological conditions. These will open up various applications in biomedical and molecular imaging with subsurface resolution down to the nanometer scale.

INTRODUCTION

A comprehensive understanding of biological structures and processes from the molecular to cellular level has become imperative. Among the many roadblocks that still exist, characterization of the complex dynamics of biological processes, especially signal pathways at nanoscale resolution, remains a formidable challenge. The existence of multiple kinetic pathways often makes these processes difficult to unravel, because the individual steps of a multistep process are typically not synchronized among molecules. Imaging molecular structures in vitro under physiological conditions provides the ability to study their molecular processes, which can have tremendous application in biological research (*1*–*5*). Advances in electron and optical microscopies have spurred tremendous growth in biological imaging. Several electron and optical imaging techniques are used to monitor the biological systems both in vitro and in vivo. These include confocal, fluorescent, and cryo-based electron microscopies. The lack of quantitative nanomechanical analyses and imaging tools poses major challenges to monitoring in vitro biomechanics.

Recent advances in molecular imaging created the possibility of achieving numerous opportunities and objectives in biomedical research, namely, (i) real-time monitoring of events at the molecular scale, (ii) imaging effects of stimulating agents and drugs at the subcellular level, (iii) assessing progression of diseases at early stages, and (iv) achieving high-speed subcellular imaging in a reproducible and quantitative manner.

There is considerable interest in using nanostructured materials as delivery vehicles (*6*), carriers, or chaperones (*7*, *8*) to interrogate cells for programmed assembly of soft, hard, and hybrid structures, among many others. The length scale of emerging nanostructures is compatible with vital biological, chemical, and physical processes, and the role of functionality of the nanoparticles [that is, light activation, radio-frequency (RF) heating, and catalytic behavior] adds an additional set of useful qualitative information to the nanostructured system. This approach to unraveling the intricate signal transduction and cellular transfection pathway includes use of taggants, such as nanoparticles, to provide spatial and temporal information about their pathway from cell wall entry to the delivery of relevant cargo inside the nucleus.

Despite recent advances, conventional imaging methods, such as light and acoustic waves, struggle to attain sub–100-nm resolution because of the classical diffraction limit. Fluorescent and confocal microscopies (*9*–*14*) are traditional ways to monitor biological interactions, but they suffer from poor spatial resolution and need fluorescent dyes. Scanning probe microscopy has made significant advances in biological imaging. It can provide very high spatial resolution but is limited to identifying surface structures and mechanical properties. Unfortunately, these methods are not capable of imaging subcellular structures (*15*–*18*). These techniques provide only the qualitative and structural information, but not the quantitative data. In summary, no single modality currently meets the needs of high sensitivity and high spatial and temporal resolution.

Quantitative nondestructive imaging methods, such as photoacoustic and light-optical microscopies, are limited by classical diffraction (*19*–*22*) and by the need of lenses, coupling fluid, relatively low resolving power, high cost, and complexity for the user. Moreover, detectability is variable-dependent. In summary, there are several advantages of confocal, fluorescent, and photoacoustic microscopies over traditional optical imaging, such as depth sensitivity and lateral and axial resolutions, but none of these technologies can provide subnanometer resolution in vitro.

During the past decade, acoustic wave–based detection methods were able to determine the mechanical properties of soft and hard materials. Because elastic strain waves can travel through different materials, without any damage to them, they can be used to noninvasively image subsurface structures, a concept that is widely used in medical imaging. The spatial resolution, that is, the smallest defect size or resolvable separation between close defects, is limited by elastic wave diffraction to a fraction of the wavelength in the far field—a distance from the defect that is several times the wavelength. Several groups used a combination of high-frequency ultrasonic waves and atomic force microscopy (AFM) to study the nanomechanics of materials and subsurface imaging, where an AFM probe was used as the local mechanical detector of elastic waves (*23*–*34*). Most of the applications focused on semiconductor and polymeric materials. Recent reports of ultrasonic imaging under physiological conditions do not demonstrate nanometer-scale resolutions because acoustic dampening in aqueous media is very challenging (*35*, *36*). Without eliminating the acoustic dampening of the cantilever, it is not possible to achieve nanoscale resolution under subcellular conditions. Moreover, imaging under physiological conditions is very challenging because of acoustic dampening of the cantilever oscillations, which limit the penetration depth, and significant advances in the technology are required to overcome these limitations.

Here, we report the development of an ultrasound bioprobe with nanometer-scale resolution for in vitro molecular imaging under

[1]Department of Materials Science and Engineering and NU*ANCE* Center, Northwestern University, Evanston, IL 60208, USA. [2]Department of Medicine, University of Illinois, Chicago, IL 60612, USA.
*Corresponding author. Email: g-shekhawat@northwestern.edu

physiological conditions while overcoming the ultrasound attenuation, with applications ranging from subcellular nanomechanical imaging of live endothelial cells (ECs) to the identification of subsurface contrast from embedded magnetic particles in silica core shells. Our results demonstrate high subsurface phase sensitivity under physiological conditions and nanomechanical imaging of subcellular structures. Our ultrasound bioprobe synergistically combines the noninvasive nature and sensitivity of deeply buried intracellular features using ultrasound waves, and a near-field AFM mechanical probe provides high phase sensitivity and mechanical contrast of the scattered ultrasound wave (*23*).

RESULTS AND DISCUSSION

Imaging in physiological media is very challenging when it comes to acoustics. Acoustic dampening in fluidics is a very common phenomenon. We developed an ultrasonic bioprobe controller that has integrated feedback electronics, which maintains the cantilever with sufficient amplitude under physiological conditions to acquire high-resolution ultrasound phase images. The feedback electronics is directly applied to the cantilever oscillations generated by the beat frequency. A judicious choice of the beats was selected to excite the cantilever contact resonance for signal amplification. If the cantilever frequency shifts during the scanning in aqueous solutions, then both the tip vibration amplitude and phase will change accordingly. This will cause a shift in the phase compensator (PC) output, bringing the voltage-controlled oscillator (VCO) to the piezo-resonance of the cantilever. This development not only prevents any offset in the cantilever piezo-resonance but also minimizes the acoustic damping in fluidics by maintaining the constant drive amplitude of the cantilever piezo. An RF amplifier was used to ramp up the dampened amplitude of the cantilevers and is more important especially with semi-viscous liquids.

In the feedback electronics design, we use a VCO that drives the tip piezo. The reference frequency signal is connected through a variable phase shifter to a PC, where it is compared with the actuator. The PC basically consists of a pair of operational amplifier comparators, an exclusive OR gate, and a low-pass filter. The PC's output is a dc correction signal that varies in accordance with the phase shift between the input signals and acts as a feedback correction signal to the VCO. If the cantilever piezo-resonance frequency shifts during the scanning, then both the tip vibration amplitude and phase will change accordingly. This will cause a shift in the PC output, bringing the VCO back to the cantilever piezo-resonance frequency.

Figure 1 depicts the schematics of the ultrasonic waves launched from both the cantilever and sample piezo. It shows the change in the phase shift when acoustic waves interact with the sample. We used a custom-made sample where the magnetic particles are in silica core. The potential application of our approach is to look through the embedded magnetic nanoparticles in silica core shells directly without going through complex transmission electron microscopy (TEM) sample preparation, which is a conventional way to look at these samples (*37*–*39*).

The silica core shell has an average diameter of 30 to 40 nm and is well dispersed on the mica surface. Figure 2A depicts the magnetic particle enclosed in the silica core shell with receptor coating around it. The normal AFM topography scan (Fig. 2B) shows a uniform distribution of silica core shell particles that spread on the mica substrate, whereas the normal tapping-mode phase image in Fig. 2C shows a typical phase image of these silica core shells. However, the ultrasound bioprobe image in Fig. 2D demonstrates the subsurface imaging capability of the system under physiological conditions with high resolution. It shows not only the embedded magnetic nanoparticles enclosed in the core shell but also the silica core shell and the receptor coating on top. The phase contrast in ultrasonic images demonstrates the capability of this technology in identifying the mechanical contrast from embedded nanoparticles with nanometer-scale resolution. The contrast in the phase image arises from the mechanical difference between the silica and cobalt nanoparticles, which results from the phase delay of the ultrasound waves coming at the sample surface. This example demonstrates the efficacy of this approach in looking through hard nanostructures and opens up an opportunity to explore noninvasive real-time tracking of cellular uptake of these core shell nanostructures with target-specific drug receptors. On the basis of the stiffness of specific materials, the contrast varies accordingly. Stiffer materials have brighter contrast than softer materials. The ultrasound phase image also identifies the receptor layer coating, which is estimated to be around 5 to 10 nm. The ultrasonic frequencies of the sample and cantilever piezo-transducers are 2.21 and 2.29 MHz, respectively. We cross-validated the silica core shell particles with TEM images to ensure that the magnetic core is within the silica, as shown in fig. S1.

In addition, we evaluate two possible contributions to image contrast from subsurface features for ultrasonic AFM methods, where both the AFM probe tip and sample are excited at ultrasonic frequencies in contact mode. The two contrast mechanisms are ultrasonic scattering from subsurface features and the differential stress field caused by subsurface feature when an AFM tip in contact generates a stress field in the sample. The ultrasonic plane waves generated at the base of the sample travel through the sample bulk. Diffraction of these waves by subsurface feature can be detected at the surface if the surface lies within the near field of this feature. Therefore, it is expected that the AFM tip generates a stress field in the sample. This stress field can be modified if there is a subsurface defect in its range. The dominant mechanism of detection will depend on the relative magnitudes of the signals and signal perturbations.

The extreme sensitivity of the probe to contact stiffness facilitates the detection of local changes in the elastic stiffness within the compressed

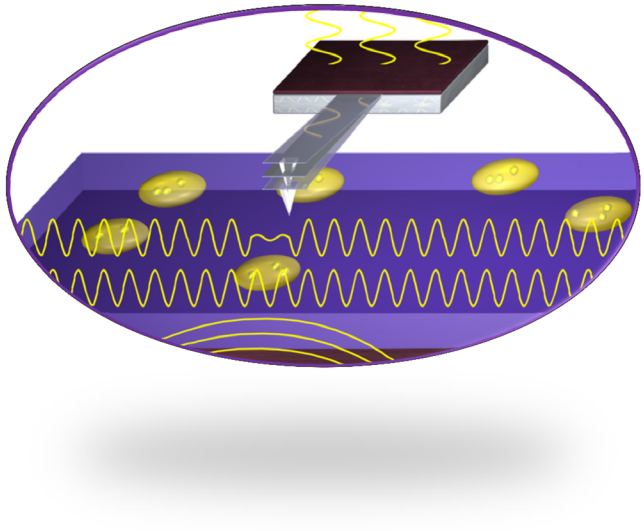

Fig. 1. Schematic illustration of an ultrasound bioprobe. Customized piezo-transducers underneath the sample and the cantilever provide the flexural vibrations. The AFM mechanical probe detects the subsurface mechanical contrast.

volume. Furthermore, the motion of the cantilever supporting the AFM probe tip depends on the sample surface displacement. Here, the mechanical AFM probe serves as the local elastic antenna, and ultrasonic vibrations are known to enhance sensitivity to local elastic properties (*40*).

Acute lung injury/acute respiratory distress syndrome (ALI/ARDS) is a devastating complication of acute respiratory failure and results in significant morbidity and mortality in critically ill patients (*41*). It is critical to understand and mechanistically characterize the pathophysiology of ALI/ARDS using an ultrasound bioprobe to mechanically probe the nanomechanics of intracellular fiber formations. The barrier function of ECs is greatly disrupted during ALI/ARDS, and understanding the nanomechanics of these barrier properties is critical in determining the recovery process.

Confocal and fluorescent microscopies have been traditionally used to image ECs and to determine the effect of stimulating agents such as thrombin on intracellular fibers, but none of these methods are able to detect the magnitude of stiffness of both intracellular fibers and the enhancement of stiffness in the nuclear region after thrombin injection. Upon addition of thrombin, the stress fiber formation toward the inner region of the ECs, that is, nuclear and cytoplasmic regions, causes cell contraction and increased elastic modulus in the central region of the cell (*42*, *43*).

Here, we used an ultrasound bioprobe and directly measured the effect of the stimulating agent thrombin on the mechanics of the intracellular fiber formation in these ECs. All the measurements were carried out under physiological conditions. The details of the sample preparation procedures are described in the study of Wang *et al.* (*44*), which focuses on the nanomechanics of ECs using the AFM system.

Figure 3 shows both topographical and ultrasound phase images of the thrombin-stimulated ECs under physiological conditions. The images were acquired after incubation with thrombin for 30 min. Long and thick intercellular fibers appear and span the gaps between cells that are induced by thrombin (phase image). These cytoskeletal fibers are predominantly visible in the phase image together with other subcellular features along the nuclei region of the cells. These results demonstrate the uniqueness of this technique to image the internal structures of the cell and those along the cell periphery. The ultrasonic frequencies of the sample and cantilever piezo-transducers are 2.20 and 2.30 MHz, respectively. We demonstrate that after the addition of thrombin, the cells exhibit increased stress fibers, indicative of contraction, and widening of intercellular gaps.

In our previous studies, we used AFM-based quantitative nanomechanics to study the stiffness variation on the intracellular region of the thrombin-treated ECs in aqueous media (*44*). AFM imaging shows the intracellular fibers but captures only the fibers that are more or less aligned with topographical images and those that are thick enough. It does not provide the contrast coming from smaller intracellular fibers and variation of stiffness in the nuclear region of the ECs, but the ultrasound bioprobe provides the subsurface stiffness contrast coming from both thicker and smaller fibers as well as from the intracellular gaps. In addition, contrast from very small fibers within the intracellular fiber network is visible in Fig. 3B. It demonstrates the technological advantages of using feedback electronics for high-resolution phase images with ultrasound. Figure S2 shows images obtained without the feedback electronics. The resolution of the ultrasound phase images is very low, and it is difficult to identify any intracellular features. Figure S3 shows

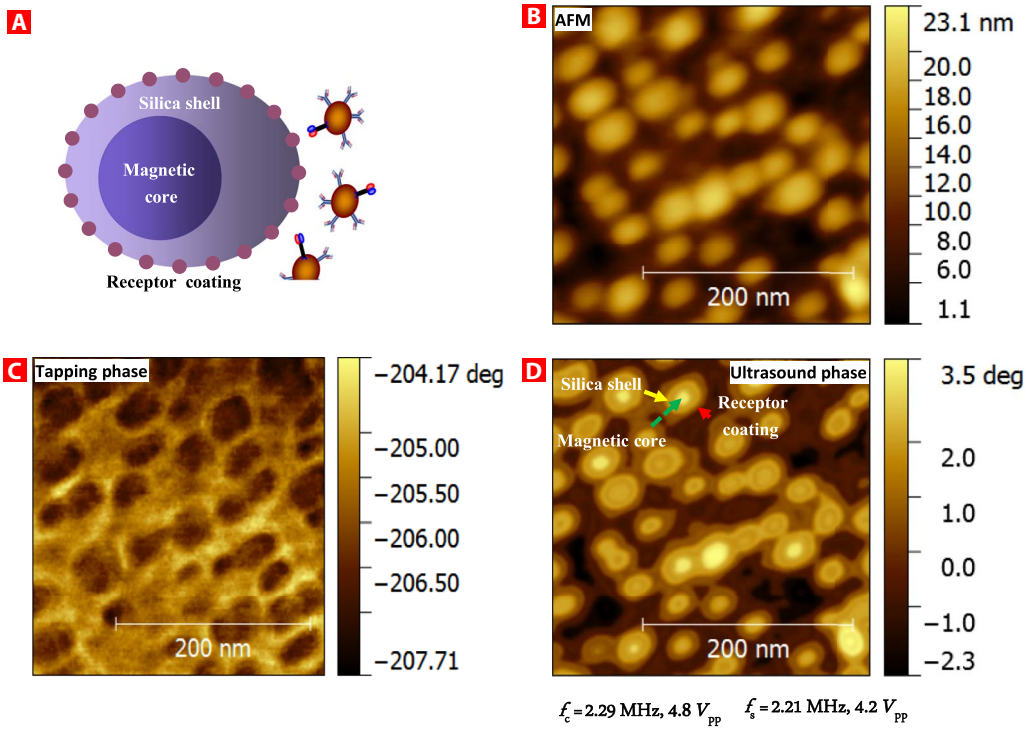

Fig. 2. Subsurface imaging of magnetic particles embeded in silica core shell. (**A**) Schematic illustration of the magnetic core nanostructure embedded in the refractory silica core shell–based molecular marker. (**B**) AFM topographical image showing well dispersed silica core shell nanostructures. (**C**) Normal tapping-mode phase image that doesn't show any phase contrast coming from embedded particles in silica core. (**D**) Phase contrast from subsurface magnetic nanoparticles enclosed in core shell nanoparticles at nanoscale spatial resolution. The magnetic core, silica core, and receptor layer are identified in the ultrasonic phase. f_s and f_c are the sample and cantilever ultrasonic frequencies, respectively.

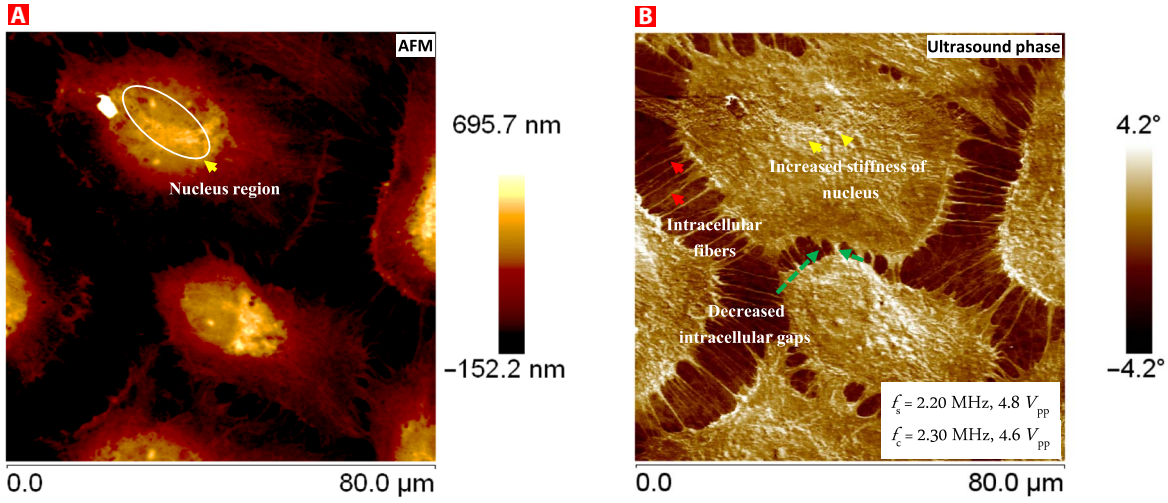

Fig. 3. Intracellular fibers imaging of endothelial cells stimulated with thrombin. (**A**) AFM topographical image of the ECs altered by the addition of thrombin. (**B**) Ultrasound bioprobe phase image showing notable contrast from intracellular fibers. Intracellular fibers are predominantly seen in the ultrasound phase image along with stretched gaps and subcellular phase contrast in the nuclear region of the cells.

the effect of the feedback controller on the amplitude of the beats when it is switched on and off. It demonstrates the significant advantage of using feedback mechanism on the cantilever oscillations to acquire high-resolution images. The beat frequency was measured with a spectrum analyzer.

Finally, the development of an ultrasound bioprobe for intracellular and in vitro molecular imaging completely opens up new applications in in vitro subcellular biological imaging with very high resolution. The representative examples of ultrasound bioprobe applications for intracellular imaging demonstrate the versatility of this technique. We believe that our technique will fill the critical void in the subnanometer spatial range for nondestructive subsurface imaging in the biological sciences.

MATERIALS AND METHODS

Experimental platform

The system incorporates a commercial contact mode AFM system (JEOL, JSPM-5200) and the Bruker Dimension Icon system. The piezoelectric transducer sample assembly is mounted on the AFM translational stage. A silicon cantilever with a spring constant of ~1.0 to 2.0 N/m, a free resonance frequency of around 75 to 125 KHz, and a nominal tip radius of 5 to 10 nm was used. We customized the AFM cantilever holder assembly that provides the flexural vibrations to the cantilever. The output of the AFM photodetector is fed to an RF lock-in amplifier to demodulate the defection of the cantilever at the difference frequency, $f = f_1 - f_2$, where f_1 and f_2 are the sinusoidal actuation frequencies of the sample and the cantilever, respectively. The reference input to the lock-in amplifier is obtained by mixing a fraction of the drive voltages to two piezoelectric transducers in an electronic mixer and by passing the output through a low-pass filter with a cutoff frequency of 1 MHz.

The sample was mounted on a piezoelectric transducer with a nominal center frequency of around 2 MHz. We used a thin film of phenyl salycilate powder heated to a transition temperature of 40°C and an adhesive layer between the sample and the transducer to enhance the transmission of elastic waves into the sample.

Silica particle growth

We used a typical synthetic approach for the specimen preparation of core shell nanoparticles. Aqueous $CoCl_2$ (0.4 M) solution was reduced using sodium borohydride in the presence of citric acid. The solution was diluted in 200 ml of water. Aminopropoxysilane (10 μl)/triethoxysilane (50 μl) (in ethanol) was slowly added to the black-colored solution by rigorous stirring. The particles were separated by centrifugation. Using this method, magnetic particles were embedded in silica core shell.

SUPPLEMENTARY MATERIALS

Supplementary material for this article is available at http://advances.sciencemag.org/cgi/content/full/3/10/e1701176/DC1

fig. S1. High-resolution TEM image of the magnetic particles embedded in the silica core shell.

fig. S2. Ultrasound bioprobe image of the ECs when treated with thrombin.

fig. S3. Detection of difference (beat) frequency when the feedback control electronics of probe is on and off.

REFERENCES AND NOTES

1. J. Y. Adams, M. Johnson, M. Sato, F. Berger, S. S. Gambhir, M. Carey, M. L. Iruela-Arispe, L. Wu, Visualization of advanced human prostate cancer lesions in living mice by a targeted gene transfer vector and optical imaging. *Nat. Med.* **8**, 891–897 (2002).
2. J. Suzuki, K. Kanemaru, K. Ishii, M. Ohkura, Y. Okubo, M. Lino, Imaging intra-organellar Ca^{2+} at subcellular resolution using CEPIA. *Nat. Commun.* **5**, 4153 (2014).
3. R. Nowakowski, P. Luckham, P. Winlove, Imaging erythrocytes under physiological conditions by atomic force microscopy. *Biochim. Biophys. Acta* **1514**, 170–176 (2001).
4. H. Shroff, C. G. Galbraith, J. A. Galbraith, E. Betzig, Live cell photoactivated localization microscopy of nanoscale adhesion dynamics. *Nat. Methods* **5**, 417–423 (2008).
5. Y. F. Dufrêne, D. Martínez-Martín, I. Medalsy, D. Alsteens, D. J. Müller, Multiparametric imaging of biological systems by force-distance curve-based AFM. *Nat. Methods* **10**, 847–854 (2013).
6. C.-H. Tung, R. Weissleder, Arginine containing peptides as delivery vectors. *Adv. Drug Deliv. Rev.* **55**, 281–294 (2003).
7. Y. Zhang, N. Kohler, M. Zhang, Surface modification of superparamagnetic magnetite nanoparticles and their intracellular uptake. *Biomaterials* **23**, 1553–1561 (2002).
8. J. W. M. Bulte, D. L. Kraitchman, Monitoring cell therapy using iron oxide MR contrast agents. *Adv. Drug Deliv. Rev.* **5**, 567–584 (2004).
9. H. Y. Au-Yeung, E. J. New, C. J. Chang, A selective reaction-based fluorescent probe for detecting cobalt in living cells. *Chem. Commun.* **48**, 5268–5270 (2012).

10. J. Chojnacki, T. Staudt, B. Glass, P. Bingen, J. Engelhardt, M. Anders, J. Schneider, B. Müller, S. W. Hell, H.-G. Kräusslich, Maturation-dependent HIV-1 surface protein redistribution revealed by fluorescence nanoscopy. *Science* **338**, 524–528 (2012).
11. H. Hama, H. Kurokawa, H. Kawano,R. Ando, T. Shimogori, H. Noda, K. Fukami, A. Sakaue-Sawano, A. Miyawaki, Scale: A chemical approach for fluorescence imaging and reconstruction of transparent mouse brain. *Nat. Neurosci.* **14**, 1481–1488 (2011).
12. O. Idevall-Hagren, E. J. Dickson, B. Hille, D. K. Toomre, P. De Camilli, Optogenetic control of phosphoinositide metabolism. *Proc. Natl. Acad. Sci. U.S.A.* **109**, E2316–E2323 (2012).
13. K. E. Kubow, A. R. Horwitz, Reducing background fluorescence reveals adhesions in 3D matrices. *Nat. Cell Biol.* **13**, 3–5 (2011).
14. K. Okabe, N. Inada, C. Gota, Y. Harada, T. Funatsu, S. Uchiyama, Intracellular temperature mapping with a fluorescent polymeric thermometer and fluorescence lifetime imaging microscopy. *Nat. Commun.* **3**, 705 (2012).
15. R. Garcia, E. T. Herruzo, The emergence of multifrequency force microscopy. *Nat. Nanotechnol.* **7**, 217–226 (2012).
16. L. Gross, Recent advances in submolecular resolution with scanning probe microscopy. *Nat. Chem.* **3**, 273–278 (2011).
17. P. E. Marszalek, Y. F. Dufrêne, Stretching single polysaccharides and proteins using atomic force microscopy. *Chem. Soc. Rev.* **41**, 3523–3534 (2012).
18. A. Raman, S. Trigueros, A. Cartagena, A. P. Z. Stevenson, M. Susilo, E. Nauman, S. A. Contera, Mapping nanomechanical properties of live cells using multi-harmonic atomic force microscopy. *Nat. Nanotechnol.* **6**, 809–814 (2011).
19. X. Cai, Y. S. Zhang, Y. Xia, L. V. Wang, Photoacoustic microscopy in tissue engineering. *Mater. Today* **16**, 67–77 (2013).
20. L. Wang, K. Maslov, L. V. Wang, Single-cell label-free photoacoustic flowoxigraphy in vivo. *Proc. Natl. Acad. Sci. U.S.A.* **110**, 5759–5764 (2013).
21. Y. Zhang, X. Cai, Y. Wang, C. Zhang, L. Li, S.-W. Choi, L. V. Wang, Y. Xia, Noninvasive photo acoustic microscopy of living cells in two and three dimensions through enhancement by a metabolite dye. *Angew. Chem.* **123**, 7497–7501 (2011).
22. Y. S. Zhang, J. Yao, C. Zhang, L. Li, L. V. Wang, Y. Xia, Optical-resolution photoacoustic microscopy for volumetric and spectral analysis of histological and immunochemical samples. *Angew. Chem. Int. Ed.* **53**, 8099–8103 (2014).
23. G. S. Shekhawat, V. P. Dravid, Nanoscale imaging of buried nanostructures via scanning near-field ultrasound holography. *Science* **310**, 89–92 (2005).
24. L. Tetard, A. Passian, R. M. Lynch, B. H. Voy, G. Shekhawat, V. Dravid, T. Thundat, Elastic phase response of silica particles buried in soft matters. *Appl. Phys. Lett.* **93**, 133113 (2008).
25. L. Tetard, A. Passian, K. T. Venmar, R. M. Lynch, B. H. Voy, G. Shekhawat, V. P. Dravid, T. Thundat, Imaging nanoparticles in cells by nanomechanical holography. *Nat. Nanotechnol.* **3**, 501–505 (2008).
26. R. E. Geer, O. V. Kolosov, G. A. D. Briggs, G. S. Shekhawat, Nanometer-scale mechanical imaging of aluminum damascene interconnect structures in a low-dielectric-constant polymer. *J. Appl. Phys.* **91**, 4549–4555 (2002).
27. Y. M. Efremov, W.-H. Wang, S. D. Hardy, R. L. Geahlen, A. Raman, Measuring nanoscale viscoelastic parameters of cells directly from AFM force-displacement curves. *Sci. Rep.* **7**, 1541 (2017).
28. O. V. Kolosov, M. R. Castell, C. D. Marsh, G. A. D. Briggs, T. I. Kamins, R. S. Williams, Imaging the elastic nanostructure of Ge islands by ultrasonic force microscopy. *Phys. Rev. Lett.* **81**, 1046–1049 (1998).
29. M. T. Cuberes, H. E. Assender, G. A. D. Briggs, O. V. Kolosov, Heterodyne force microscopy of PMMA/rubber nanocomposites: Nanomapping of viscoelastic response at ultrasonic frequencies. *J. Phys. D: Appl. Phys.* **33**, 2347 (2000).
30. S. A. Cantrell, J. H. Cantrell, P. T. Lillehei, Nanoscale subsurface imaging via resonant difference-frequency atomic force ultrasonic microscopy. *J. Appl. Phys.* **101**, 114324 (2007).
31. O. Kolosov, UFM shakes out the details at the nanoscopic scale. *Mater. World* **6**, 753–754 (1998).
32. G. Shekhawat, A. Srivastava, S. Avasthy, V. Dravid, Ultrasound holography for noninvasive imaging of buried defects and interfaces for advanced interconnect architectures. *Appl. Phys. Lett.* **95**, 263101 (2009).
33. S. Avasthy, G. Shekhawat, V. Dravid, Scanning Near field ultrasound holography, in *Encyclopedia of Analytical Chemistry*, R. Meyers, Ed. (John Wiley and Sons Ltd., 2010).
34. G. S. Shekhawat, S. Avasthy, A. K. Srivastava, S.-H. Tark, V. P. Dravid, Probing buried defects in extreme ultraviolet multilayer blanks using ultrasound holography. *IEEE T. Nanotechnol.* **9**, 671–674 (2010).
35. M. Ewald, L. Tetard, C. Elie-Caille, L. Nicod, A. Passian, E. Bourillot, E. Lesniewska, From surface to intracellular non-invasive nanoscale study of living cells impairments. *Nanotechnology* **25**, 295101 (2014).
36. P. Vitry, R. Rebois, E. Bourillot, A. Deniset-Besseau, M.-J. Virolle, E. Lesniewska, A. Dazzi, Combining infrared and mode synthesizing atomic force microscopy: Application to the study of lipid vesicles inside *Streptomyces* bacteria. *Nano Res.* **9**, 1674–1681 (2016).
37. M. Aslam, S. Li, V. P. Dravid, Controlled synthesis and stability of Co@SiO_2 aqueous colloids. *J. Am. Ceram. Soc.* **90**, 950–956 (2007).
38. S. C. McBain, H. H. Yiu, J. Dobson, Magnetic nanoparticles for gene and drug delivery. *Int. J. Nanomedicine* **3**, 169–180 (2008).
39. J. Dobson, Magnetic micro- and nano-particle–based targeting for drug and gene delivery. *Nanomedicine* **1**, 31–37 (2006).
40. Z. Parlak, F. L. Degertekin, Contact stiffness of finite size subsurface defects for atomic force microscopy: Three-dimensional finite element modeling and experimental verification. *J. Appl. Phys.* **103**, 114910 (2008).
41. G. D. Rubenfeld, E. Caldwell, E. Peabody, J. Weaver, D. P. Martin, M. Neff, E. J. Stern, L. D. Hudson, Incidence and outcomes of acute lung injury. *N. Engl. J. Med.* **353**, 1685–1693 (2005).
42. J. G. N. Garcia, F. Liu, A. D. Verin, A. Birukova, M. A. Dechert, W. T. Gerthoffer, J. R. Bamberg, D. English, Sphingosine 1-phosphate promotes endothelial cell barrier integrity by Edg-dependent cytoskeletal rearrangement. *J. Clin. Investig.* **108**, 689–701 (2001).
43. S. M. Dudek, J. R. Jacobson, E. T. Chiang, K. G. Birukov, P. Wang, X. Zhan, J. G. N. Garcia, Pulmonary endothelial cell barrier enhancement by sphingosine 1-phosphate: Roles for cortactin and myosin light chain kinase. *J. Biol. Chem.* **279**, 24692–24700 (2004).
44. X. Wang, R. Bleher, M. E. Brown, J. G. N. Garcia, S. M. Dudek, G. S. Shekhawat, V. P. Dravid, Nano-biomechanical study of spatio-temporal cytoskeleton rearrangements that determine subcellular mechanical properties and endothelial permeability. *Sci. Rep.* **5**, 11097 (2015).

Acknowledgments: This work used the Scanned Probe Imaging and Development facilities of the NU*ANCE* Center at Northwestern University, which received support from the Soft and Hybrid Nanotechnology Experimental (SHyNE) Resource, the Materials Research Science and Engineering Centers (MRSEC) program (NSF DMR-1121262) at the Materials Research Center; the International Institute for Nanotechnology (IIN); the Keck Foundation; and the State of Illinois through the IIN. We acknowledge M. Aslam for providing us with silica core shell samples and for constructive discussions. **Funding:** This study was funded by the SHyNE Resource (NSF ECCS-1542205), the MRSEC program (NSF DMR-1121262), NSF Award No. 1256188, Instrumentation Development for Biological Research (IDBR): Development of Higher Eigenmode Ultrasound Bioprobe for Sub-Cellular Biological Imaging, and the NIH National Heart Lung Blood Institute (grants P01 HL 58064 to S.M.D. and R56 HL HL56088144-06A1 to S.M.D.). **Author contributions:** G.S. designed and executed the experiments and the feedback circuit development, wrote the paper, and was responsible for Fig. 2. S.M.D. cultured the ECs and transfected them with stimulating agents, provided data analysis, wrote the manuscript, and was responsible for Fig. 3. V.D. provided design of the experiment, edited the paper, performed image analysis, and was responsible for Fig. 1. **Competing interests:** The authors declare that they have no competing interests. **Data and materials availability:** All data needed to evaluate the conclusions in the article are present in the article and/or the Supplementary Materials. Additional data related to this paper may be requested from the authors.

Submitted 12 April 2017
Accepted 22 September 2017
Published 25 October 2017
10.1126/sciadv.1701176

Citation: G. S. Shekhawat, S. M. Dudek, V. P. Dravid, Development of ultrasound bioprobe for biological imaging. *Sci. Adv.* **3**, e1701176 (2017).

Science Advances

Development of ultrasound bioprobe for biological imaging

Gajendra S. Shekhawat, Steven M. Dudek and Vinayak P. Dravid

Sci Adv **3** (10), e1701176.
DOI: 10.1126/sciadv.1701176